

École Polytechnique Fédérale de Lausanne

Two degree-of-freedom tail-fin mechanism for efficient and agile
robotic fish undulatory swimming

by Gabriel Veigas Marques

Master Thesis

Prof. Josie Hughes
Thesis Professor

Nana Obayashi & Kyle Walker
Thesis Supervisor

EPFL CREATE Lab – Computational Robot Design & Fabrication Lab
EPFL STI IGM CREATELab
ME C1 365 (Bâtiment ME)
CH-1015 Lausanne

July 11, 2025

Abstract

This study investigates whether adding one actively controlled degree of freedom (DOF) at the caudal fin of a 1 m tendon-driven robotic fish can improve propulsion efficiency and manoeuvrability compared with a conventional single-DOF tail. The robot was tested in a 2.5 m tank across 48 combinations of tail-beat frequency (0.5-2 Hz) and tip amplitude (15°- 60°), first with the fin fixed, then with an active -90° phase lag, followed by a seven-point phase sweep and two families of turning manoeuvres. Results show that the dual-DOF configuration increased peak cruising speed from 0.18 m/s to 0.25 m/s, lowered cost of transport from ≈ 10 to 6 J/kg·m at optimal gait, and nearly doubled peak yaw rate in gliding turns (28 deg/s vs 14 deg/s). A tail-leading phase of -30° to -60° maximised both speed and economy, while fin-leading phases were detrimental. Despite these gains the robot still operated at Strouhal numbers 4–10 × higher than biological optima because of drag from its exposed skeleton and tank confinement, highlighting opportunities for streamlined skins and closed-loop fin control. The findings confirm that a modest second DOF can significantly enhance robotic fish performance and lay groundwork for more efficient, agile bio-inspired AUVs.

Contents

Abstract	2
1 Introduction	5
2 Literature Review	7
3 Robot Description	11
3.1 General Dimensions and Variables	11
3.2 Skeleton and Kinematics	12
3.2.1 Qualitative motion description	12
3.2.2 Tail-bending kinematics	13
3.2.3 Fin-pitch kinematics	15
3.3 Electronics and Firmware	16
4 Methods	18
4.1 Experimental set-up	18
4.2 Test matrices	19
4.2.1 Strouhal sweep	19
4.2.2 Phase-Coupling Study	19
4.2.3 Turning manoeuvres	20
4.3 Data processing	20
4.3.1 Data synchronisation, tracking and kinematic extraction	20
4.3.2 Electrical power and cost of transport	21
4.3.3 Performance metrics	21
5 Results	23
5.1 Propulsive Efficiency and Strouhal Number	23
5.1.1 Amplitude and frequency sweep	23
5.1.2 Strouhal and efficiency	25
5.2 Effect of Fin–Body Phase Lag	26
5.3 Maneuverability Tests	27
5.3.1 Gliding Turns	27

5.3.2 Swimming Turns	28
6 Discussion	31
6.1 Steady Swimming: 2DOF Advantage and Strouhal Analysis	31
6.2 Maneuverability and Gait Modulation	33
7 Conclusion	35
Bibliography	37

Chapter 1

Introduction

Efficient, low-disturbance propulsion is a primary goal for autonomous underwater vehicles (AUV) that must travel long distances, cruise for hours, and collect data without altering the environment they survey. Conventional craft pursue that goal with propellers. Although robust and simple, a propeller converts only the axial component of the induced flow into thrust, while radial outflow, hub vortices, and high-tip speed cavitation waste energy, accelerate wear and create acoustic disturbances. Studies show that propeller powered AUVs have a much higher Cost of Transport (CoT) compared to marine life [1, 2]. Each drawback shortens mission endurance or degrades data quality.

Natural swimmers offer a different solution. Most fish and aquatic mammals generate thrust by sending a travelling bending wave down a compliant body-tail structure, redirecting water into a narrow jet with minimal swirl. Hundreds of millions of years of evolutionary iterations have optimized this gait for energy efficiency. Laboratory foils, high-speed video of live fish, and recent robotic prototypes show that propulsive efficiency collapses onto a single non-dimensional parameter, the Strouhal number.

$$St = \frac{2Af}{U} \quad (1.1)$$

Where A is peak lateral tail amplitude, f is tail-beat frequency, and U is forward speed. Efficiency peaks inside the tight band $0.25 < St < 0.35$ [3]. Outside this window additional thrust comes with an energetic penalty.

The hypothesis is that adding a second, independently controlled degree of freedom (DoF) will improve thrust control, maneuverability, and ultimately Cost of Transport compared with a single-DOF pitching tail. A one-meter prototype whose tail motor sets the body wave, while a separate fin motor applies a programmable phase lead or lag was built in order to test that hypothesis.

By sweeping beat frequency and amplitude the robot still operates across the Strouhal window $0.25 < St < 0.35$; the key question is whether the extra DOF reduces CoT and tightens turns enough to offset its added mass, power draw, and control complexity. The robot's anatomy mimics vertebral flexion and fin rotation of large fishes or sharks, yet remains stiff about unwanted axes to maintain stability and steerability.

The study tests three hypotheses. First, multiple tail-beat frequencies and amplitudes will be tested in order to map CoT against Strouhal number and locating the efficiency optimum. Second, different phases between body curvature and fin pitch will be tested to measure how timing influences thrust and energy draw. Third, maneuverability will be studied through gliding, ratchet and power turns, recording turning radius and peak yaw rate with overhead video tracking. Speed, position, and electrical power will be logged synchronously, allowing direct calculation of CoT for every trial.

Should the robot achieve a lower or comparable CoT within the target band while maintaining agile turning, the study will analyze if adding an additional DOF allows for better overall performances than single DOF robotic fishes.

Chapter 2

Literature Review

Biological Swimming Gaits Fish swimming via body-caudal fin (BCF) propulsion is traditionally categorized into four locomotor gaits: anguilliform, sub-carangiform, carangiform, and thunniform [4]. These modes form a kinematic spectrum defined by how much of the body undulates during steady swimming. In anguilliform swimmers (e.g. eels, lampreys), undulatory waves extend along the entire trunk and tail, often with more than one wave present on the body at once. Such fish are elongated and flexible, enabling high maneuverability in complex environments at the cost of lower top speeds. On the opposite, thunniform swimmers (e.g. tuna, some lamnid sharks) keep the body rigid and restrict oscillations to the caudal peduncle and lunate tail [5]. This particularity enhances thrust efficiency and sustained speed but reduces maneuverability [6]. Sub-carangiform and carangiform modes lie between these extremes. Sub-carangiform fish (e.g. trout, cod) undulate mainly the rear half to two-thirds of the body, with increasing wave amplitude toward the tail. Carangiform swimmers (e.g. jack mackerel, many sharks) undulate the last third of the body, producing rapid tail oscillations (*source*). In both cases, the head and trunk move only slightly, while the tail stroke is pronounced.

The anatomical and hydrodynamic characteristics of these gaits correlate with propulsion efficiency. Anguilliform swimmers use extensive body motion, which can waste energy as lateral recoil instead of forward thrust. Their propulsive efficiencies are moderate (on the order of 50–70% in experiments and simulations) [7], sufficient for low-speed cruising and navigating tight spaces. As undulation becomes more concentrated caudally (sub-carangiform → carangiform → thunniform), propulsive efficiency tends to improve [6]. Carangiform swimmers achieve higher cruising speeds and efficiencies than anguilliform swimmers by minimizing unnecessary body flexure. In one comparative study, a carangiform kinematics model reached a maximum efficiency of 86%, versus 71% for an anguilliform model [7]. Thunniform swimmers are the most efficient BCF propulsors: their stiff, streamlined bodies and high-aspect-ratio lunate tails maximize thrust while reducing lateral drag [8]. Tunas and certain sharks exemplify thunniform design, cruising long distances near the optimal hydrodynamic regime. This efficiency comes at the expense of agility, tunas

cannot perform tight turns as easily as eels, illustrating a classic trade-off between speed and maneuverability in fish locomotion. Figure 2.1 summarizes the differences in body waveform and bending amplitude for anguilliform, sub-carangiform, carangiform, and thunniform swimmers.

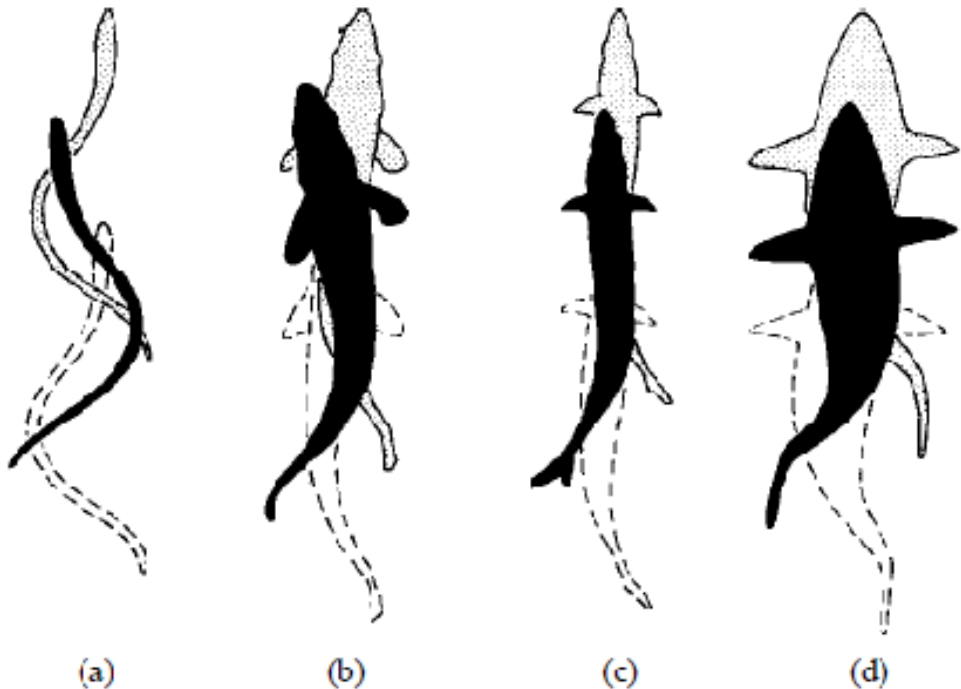


Figure 2.1: Fish classification due the locomotion mode. (a) Anguilliform, (b) subcarangiform, (c) carangiform and (d) thunniform. [4]

Strouhal Number, Amplitude Envelope, and Frequency Scaling Fish and other oscillatory swimmers achieve peak propulsive efficiency within a narrow range of kinematic parameters, often characterized by the Strouhal number (St). The Strouhal number is a dimensionless parameter defined as $St = f \cdot A/U$, where f is the tail-beat frequency, A is the characteristic oscillation amplitude (often taken as peak-to-peak), and U is the forward swimming speed. Triantafyllou et al. found that fish of various sizes (from small fish to sharks) consistently swim with St in the range of 0.25–0.35 [9]. Within this range, often called the optimal Strouhal window, the formation of vortex wakes is tuned for maximum thrust relative to input energy. Propulsive efficiency tends to peak when $0.2 < St < 0.4$, aligning with the observed kinematics of efficient swimmers. Operating outside this range (too low or too high St) results in either wasted energy (ineffective small oscillations) or the production of disorganized turbulent wakes. Thus, Strouhal tuning is a principle in which fish modulate frequency and amplitude to remain in the efficient vortex-shedding regime.

In steady swimming, fish appear to follow scaling laws for tail motion that maintain favorable Strouhal numbers across sizes and speeds. One key observation is that tail-beat amplitude often

scales with body length. In Bainbridge's classic trout and goldfish study (1958) amplitude grew with frequency up to ≈ 5 Hz, then plateaued at $0.2 L$. Beyond that point fish increased speed mainly by raising frequency while amplitude remained fixed. This pattern implies a strategy of moderate, near-constant amplitude with adaptive frequency: maintaining a bounded lateral excursion limits drag, while higher flapping rate delivers extra thrust when required. These kinematic rules help keep St in the efficient 0.2–0.4 window. Tail-beat frequency at cruise declines with body size, muscle-based scaling predicts small (< 0.5 m) swimmers can sustain 5–20 Hz whereas 1+ meter fish cruise near 1–3 Hz, with larger absolute amplitudes compensating for lower frequency.

Understanding these biological scaling laws informs hypotheses for the robotic fish trials. One hypothesis is that a robotic fish of ≈ 1 m length should likewise operate near $St \approx 0.3$ for peak efficiency, which could be achieved by selecting a combination of tail oscillation frequency and amplitude that mirror real fish proportions. For instance, if the robot's tail amplitude is set to $\approx 0.2 L$ (a biologically inspired envelope), we would predict an optimal frequency on the order of 1–3 Hz to hit the target Strouhal at cruising speeds. By grounding the robot's gait parameters in proven biological regimes, the aim is to demonstrate how deviations around the optimal range affect performance and efficiency.

Body–Caudal-Fin Phase Coupling Unlike a simple oscillating foil, real fish often have multiple degrees of freedom in their tail region: the body's tail end (peduncle) and the caudal fin can move independently. Body–caudal-fin phase coupling refers to the timing relationship between the body's undulatory wave and the motion of the caudal fin. Studies of fish kinematics (e.g. in crucian carp and bluegill sunfish) have noted that the caudal fin does not merely trail passively behind the body wave; instead, the fin can lead or lag the body's motion by a certain phase angle. In practical terms, the fin may flick at a slightly earlier phase than the tail base, creating a cupping or flipping motion that captures the energy of the body's wake. In crucian carp, it has been hypothesized that a delayed body bend followed by a quick fin flick can augment the momentum transfer to the water, effectively “pushing off” shed vortices for extra thrust during maneuvers. This is supported by hydrodynamic analyses showing that certain phase differences between body and fin motion yield constructive interference in the wake, whereas in-phase motion might waste some energy [10].

From a hydrodynamics perspective, having the caudal fin move out-of-phase can improve the wake symmetry and vortex shedding timing. A slight phase lead by the fin can mean that when the body's lateral motion generates a starting vortex, the fin's motion immediately redirects or reinforces that flow instead of being dragged in it. This coordination can result in a stronger, more axially aligned jet in the wake, which corresponds to higher thrust and efficiency [8]. The benefits are not only in straight-line thrust, they also manifest in better lateral stability and control because the fin's timing counteracts some of the body's unwanted lateral forces. Lu et al. (2024) implemented multiple flexible joints along a robotic fish tail and optimized their phase differences for performance. They demonstrated that proper phasing substantially reduces the cost of transport, in their case by up to 81% relative to an otherwise identical robot without phase-optimized tail motion [11].

Turning and Maneuverability Beyond steady swimming, fish locomotion includes rapid maneuvers that demand different kinematics. C-starts are a good example: a sudden escape turn where the fish's body contorts into a C-shape, then unwinds violently to propel the animal away from a threat [5]. C-start maneuvers achieve extremely high angular accelerations and short response times (tens of milliseconds), but they are energetically costly and mechanically stressful. Another category of turning is more gradual, often named gliding turns or banking turns. In a gliding turn, a fish may roll its body slightly and use its fins (e.g. pectoral, dorsal, anal or caudal fins) as rudders, executing a smoother change of heading with minimal loss of speed. Certain species (like trout or sharks) combine body bending with subtle fin adjustments to achieve such banked turns, maintaining stability by distributing forces across multiple fins [5]. Previous robotic fish have implemented maneuvers using various approaches. Some early designs performed C-start-like flicks with a single tail joint, essentially whipping the tail to induce a turn. This produces quick results but lacks finesse and often destabilizes the robot.

The tendon-driven robotic fish can exploit its dual-DOF tail for better maneuverability. The ability to control the caudal fin's orientation independently opens up new possibilities. Using the joint effects of the tail bending and the caudal fin to test three different turning gaits: gliding turns, power turns and ratchet turns.

Chapter 3

Robot Description

This chapter documents the mechanical architecture, embedded electronics and the software structure of *RoboFish-1m*.

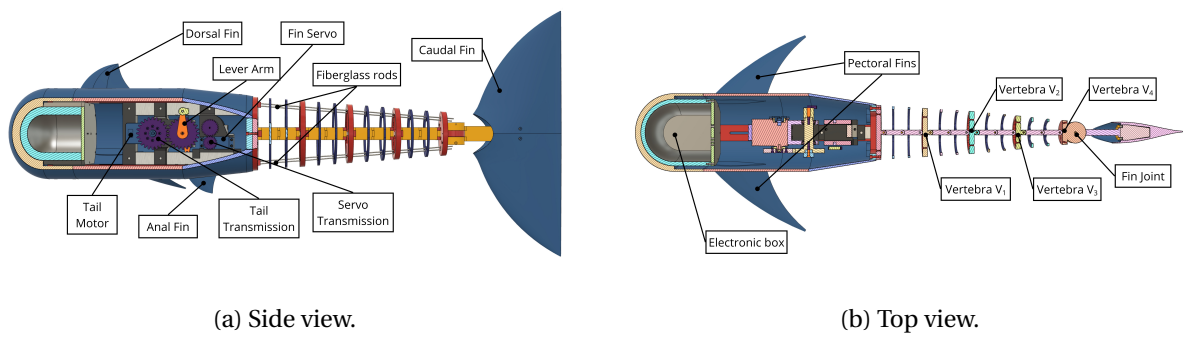


Figure 3.1: Orthogonal projections of *RoboFish-1m*.

3.1 General Dimensions and Variables

Table 3.1a lists the principal dimensions and masses of the prototype. Values refer to the AUV in working configuration with batteries and payload installed. Table 3.1b refers to the variable related to the motion.

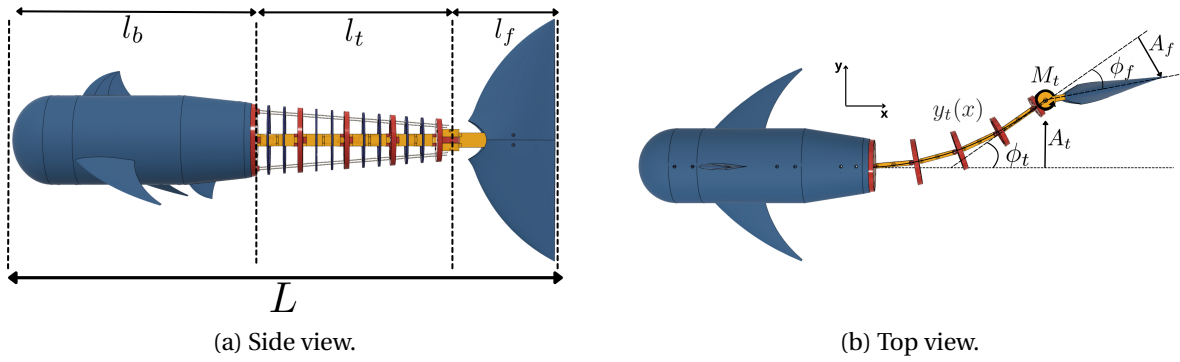


Figure 3.2: Orthogonal projections of *RoboFish-1m*.

Table 3.1: Principal dimensions and variables of *RoboFish-1m*

(a) Dimensions and constants			(b) Variables		
Parameter	Symbol	Value	Variable	Symbol	Range
Overall length	L	1.037 m	Tail beat freq.	f	[0,2] Hz
Rigid body length	l_b	0.551 m	Tail amplitude	A_t	$\approx [-220, 220]$ mm
Flexible tail length	l_t	0.324 m	Tail beat angle	ϕ_t	$[-78^\circ, 78^\circ]$
Fin length	l_f	0.162 m	Fin angle amplitude	ϕ_f	$[-\frac{\pi}{3}, \frac{\pi}{3}]$ rad
Caudal-fin span	b_f	0.4 m	Phase lag (tail-fin)	φ	$[-\frac{\pi}{2}, \frac{\pi}{2}]$ rad
Lever arm	l_{arm}	35 mm			
Fiberglass rod diameter	d_r	2 m			
Tendon attachment offset	e	15 mm			
Gear ratio (tail axis)	G_t	1:1			
Gear ratio (fin axis)	G_f	21:26			
Dry mass	m_{dry}	2.335 kg			
Wet mass	m_{wet}	8.640 kg			
Battery capacity	E_{bat}	1.6 Ah			
Fiberglass flex. modulus	E_{fg}	30 GPa			

3.2 Skeleton and Kinematics

3.2.1 Qualitative motion description

The robot is composed of a rigid forward hull and a eight-joint flexible spine allowing compliance in the plane in which bending occurs while constraining torsion and out of plane movements (Fig. 3.3). Motion is decomposed into two orthogonal degrees of freedom:

- **Tail flexion.** Four fibreglass rods lie in the horizontal mid-plane, pictured in green in the figure 3.3 . A pair of antagonistic Dyneema tendons attaches to an offset of 15 mm from the centreline on the terminal vertebra V_4 . Pulling on one tendon and releasing the other yields a bending moment M_t producing a flexion of the fiberglass rods. The motion of the tail is analogous to a fixed-end beam bending.
- **Caudal-fin rotation.** The servo motor drives a bidirectional pulley. Two antagonistic Dyneema run from the pulley to the base of the caudal fin through the centerline of the tail. It allows a precise position control of the caudal fin even under load.

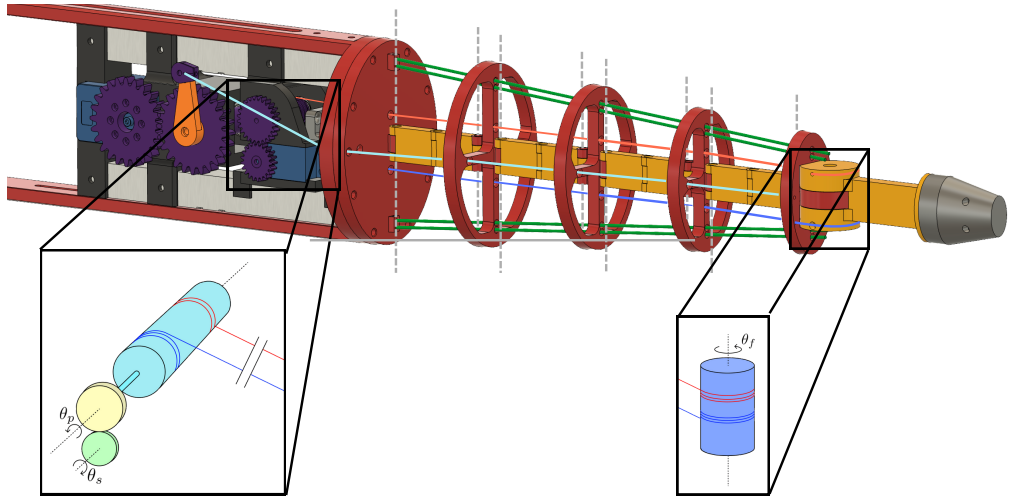


Figure 3.3: Detailed view of the skeleton of the tail. Key components are highlighted in colors. Lever in orange. Left tail tendon in light blue. Caudal fin tendons in red and blue. The eight spine joints axis are in light gray.

3.2.2 Tail-bending kinematics

Theoretical kinematics The four 2 mm-diameter fibreglass rods lie in a common horizontal plane; they bend only about the vertical axis. The tail therefore behaves like a single Euler–Bernoulli cantilever of length l_t and equivalent flexural rigidity

$$EI_{\text{eq}} = 4EI_{\text{rod}},$$

where E is the Young modulus of the rod material and $I_{\text{rod}} = \pi d_r^4/64$ is the second moment of area of one rod ($d_r = 2\text{ mm}$).

A differential tendon tension $\Delta T = T_{\text{port}} - T_{\text{star}}$ acting on the lever arm $e = 15\text{ mm}$ at the last

vertebra produces a tip moment

$$M_t = \Delta T e.$$

With a pure end moment and no transverse load, the curvature γ is uniform along the whole length:

$$\gamma = \frac{M_t}{EI_{\text{eq}}} \implies y_t(x) = \frac{M_t}{2EI_{\text{eq}}} x(L_t - x), \quad 0 \leq x \leq l_t.$$

The resulting tip deflection and tip slope are

$$A_t = y_t(L_t) = \frac{M_t L_t^2}{8EI_{\text{eq}}}, \quad (3.1)$$

$$\phi_t = \left. \frac{dy_t}{dx} \right|_{x=l_t} = \frac{M_t L_t}{2EI_{\text{eq}}}. \quad (3.2)$$

Equations (3.1)–(3.2) give a direct mapping from tendon preload to tail amplitude. Additional tension to pull the cables is a direct result of hydrodynamic loading and frictional losses across the composite design.

Empirical calibration. The composite spine deviates from the ideal cantilever model once large curvatures introduce friction and joint clearance. To capture these effects an empirical motor–tail map was generated: the tail motor was stepped through thirty-six uniformly spaced commands $\theta_m^{(i)} \in [-80^\circ, +80^\circ]$. For every step the resulting tip deflection $A_t^{(i)}$ and tip slope $\phi_t^{(i)}$ were recorded with an overhead camera and a calibration grid. A least-squares *cubic* fit,

$$\begin{bmatrix} A_t \\ \phi_t \end{bmatrix} = \mathbf{C} \begin{bmatrix} 1 \\ \theta_m \\ \theta_m^2 \\ \theta_m^3 \end{bmatrix}, \quad \mathbf{C} = \begin{bmatrix} 0 & 4.846 & 0 & -3.26 \times 10^{-4} \\ 0 & 1.277 & 0 & -5.22 \times 10^{-5} \end{bmatrix},$$

reproduces the measurements with $R^2 = 0.998$ ($\leq 0.03\text{mm}$ error) for amplitude and $R^2 = 1.000$ ($\leq 0.02^\circ$ error) for tip angle. During experiments every commanded servo angle is therefore converted to physical tail amplitude and angle through the calibrated coefficients \mathbf{C} ; Strouhal number and phase lag are thus computed from true kinematics rather than idealised geometry.

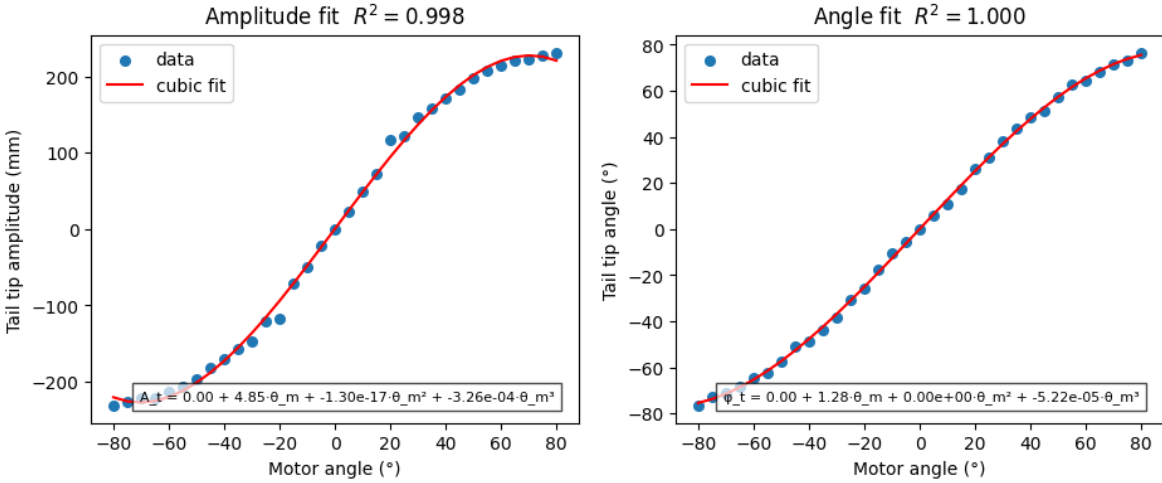


Figure 3.4: Cubic calibration of motor angle θ_m to tail-tip amplitude A_t and tip angle ϕ_t .

3.2.3 Fin-pitch kinematics

The caudal fin rotates about its spanwise axis through a three-element gear–pulley–tendon transmission (Fig. 3.3):

$$\theta_s \xrightarrow{G_g} \theta_p \xrightarrow{r_{\text{in}}} \Delta\ell \xrightarrow{r_{\text{out}}} \phi_f.$$

1. The servo carries a *21-tooth* spur gear that meshes with a *26-tooth* gear rigidly attached to the input pulley. With $G_g = \frac{N_{\text{in}}}{N_{\text{out}}} = \frac{21}{26} = 0.808$, the output gear angle is

$$\theta_p = G_g \theta_s.$$

2. The gear and its pulley share a shaft; the pulley has a radius $r_{\text{in}} = 7.25 \text{ mm}$. Shaft rotation converts directly to antagonistic tendon displacement

$$\Delta\ell = r_{\text{in}} \theta_p.$$

3. The tendons wrap the fin-root pulley $d_{\text{out}} = 34.5 \text{ mm}$ ($r_{\text{out}} = 17.25 \text{ mm}$), so the fin angle becomes

$$\phi_f = \frac{\Delta\ell}{r_{\text{out}}} = \frac{r_{\text{in}}}{r_{\text{out}}} G_g \phi_s.$$

With $r_{\text{in}}/r_{\text{out}} = 0.420$ and $G_g = 0.808$, the overall transmission factor is $K_\theta = 0.34$. A $\pm 180^\circ$ servo stroke therefore yields a fin sweep range of $\theta_f \approx \pm 60^\circ$.

Firmware introduces a programmable phase offset φ between tail tip angle and fin pitch, allowing experimental scans over $\varphi \in [-90^\circ, +90^\circ]$. The antagonistic tendon pair ensures equal slack is released on one side whenever the opposite side is tensioned, eliminating backlash at the hinge and keeping precise positioning even under hydrodynamic load during undulatory gait.

3.3 Electronics and Firmware

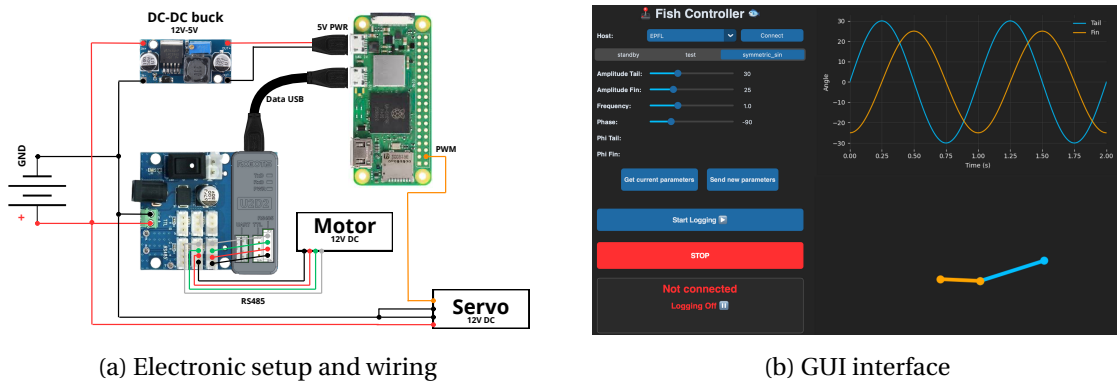


Figure 3.5

Figure 3.5a shows the embedded stack. A single 3s1p Li-Po pouch cell (12 V, 1.6 Ah) is split into two power rails:

- A 12 V bus that supplies the Dynamixel tail motor (through a Robotis U2D2 USB–RS-485 adapter) and the servo that rotates the caudal fin.
- A 5 V bus that powers the Raspberry Pi Zero 2W, which handles all real-time control and logging—no auxiliary micro-controller is required.

There is no auxiliary Microcontroller Unit, the Raspberry Pi executes all timing, kinematics and logging.

Control and user interface : At power-up the Pi launches a single C++ daemon (fish_control). Every 50 ms the loop :

1. reloads a YAML config file (cfg.yaml),
2. converts the requested tail/fin kinematics to actuator commands,
3. streams position, current and bus-voltage to a CSV log, and

- trips a watchdog restart if either the RS-485 or GPIO layer stops responding.

Because the C++ control loop watches `cfg.yaml` continuously, parameters can be edited live over Wi-Fi: the operator connects via SSH and either edits the file directly or uses the lightweight Python/Tk GUI shown in Fig. 3.5b. The GUI previews the commanded waveforms, toggles data-logging, and provides an emergency “Stop” that forces the robot into a safe-idle mode, all without opening the hull.

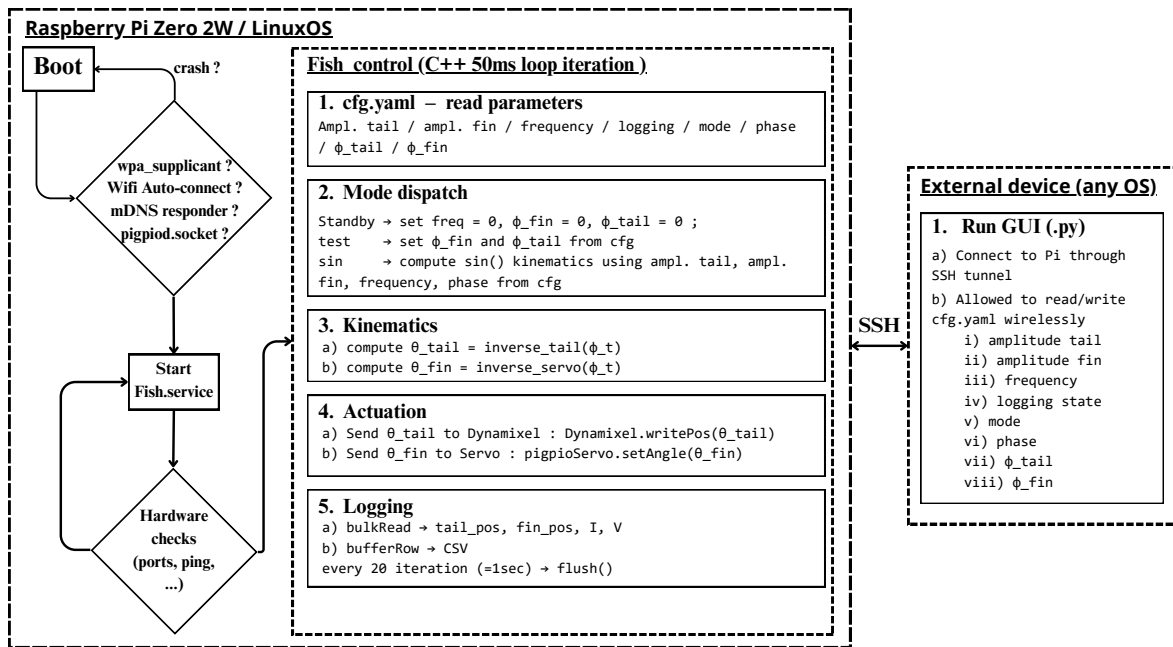


Figure 3.6: Firmware structure

The complete firmware, GUI are open-source at <https://github.com/Gabos111/fish-control.git>

Chapter 4

Methods

4.1 Experimental set-up

All trials were conducted in a soft-wall polyethylene pool measuring 248 cm (long axis) by 147 cm (short axis) and 65 cm water depth [4.1](#). The robot swims in the mid-plane of the tank and is always at least one body length from the walls to avoid ground or wall effects ($Re \approx 1.2 \times 10^4$ at the highest speed).



Figure 4.1: Overhead camera view of the experimental pool: a bio-inspired robotic fish with a pink buoyancy module swims along the centreline, while AprilTag markers fixed to the pool frame provide geometric calibration for the vision system.

A single Raspberry Pi Zero 2 W on board *RoboFish-1m* executes the `fish_control` firmware ([§3.3](#)). An SSH tunnel from a client allows live editing of `cfg.yaml`, turning on/off logging and

downloading CSV files after each run. Electrical power draw is sampled at control loop rate (20 hz). The pool is filmed from overhead with a Logitech PC-LM1E webcam (1280×720 px, 29.97 fps). The camera is rigidly fixed to a truss spanning the long axis and orthogonally aligned with the water surface. Spatial scale is calibrated once per session using a checkerboard of known size laid on the water.

A timing LED on GPIO 26 turns **ON** for exactly 5 s when logging starts; its HIGH/LOW state is appended as the last column of every CSV row so video frames and power data can be aligned to within one frame leading to a maximum synchronization error of ≤ 33 ms.

4.2 Test matrices

4.2.1 Strouhal sweep

Straight swimming was characterised over the two-dimensional grid

$$(\phi_t, A_t) \in \{(15^\circ, 56\text{ mm}), (30^\circ, 112.1\text{ mm}), (45^\circ, 164.1\text{ mm}), (60^\circ, 208.5\text{ mm})\}$$

$$f \in \{0.50, 0.75, 1.00, 1.25, 1.50, 2.00\} \text{ Hz.}$$

Two conditions below were executed at every grid point:

1. **Fixed fin.** The caudal fin servo remained at its neutral position ($\phi_f = 0^\circ$).
2. **Active fin.** The fin traced the same sine wave as the tail but with a constant -90° phase lag ($\varphi = -\frac{\pi}{2}$).

The full sweep was done 2 times, therefore comprises 48 distinct runs executed twice. Each run is long enough for the fish to cross the pool and reach steady speed just before hitting pool wall.

4.2.2 Phase-Coupling Study

The (A_t, f) pair that has the best performance and the minimum cost of transport in the Strouhal sweep is adopted as the baseline. With that pair fixed the fin phase offset is varied over

$$\varphi \in \{-90^\circ, -75^\circ, -60^\circ, -45^\circ, -30^\circ, -15^\circ, 0^\circ, 15^\circ, 30^\circ, 45^\circ, 60^\circ, 75^\circ, 90^\circ\},$$

The resulting cruising speed and cost of transport reveal the performance and energetic landscape versus phase lag.

4.2.3 Turning manoeuvres

Gliding turns. Three separate test sets isolate the contribution of each actuator in gliding turns, the following offsets were tested:

$$A_t, A_f \in \{15^\circ, 30^\circ, 45^\circ, 60^\circ\}$$

where A_t is the peak tail-wave amplitude and A_f the fin bias that can be applied as a static offset. Using that four-point amplitude grid, three experiments are executed:

1. **Tail-only sweep** : the fish is driven with the tail-wave test set (A_t) while the caudal fin remains neutral ($\phi_f = 0^\circ$).
2. **Fin-only sweep** : the tail is disabled; each fin bias from the same test set (A_f) is imposed as a constant deflection.
3. **Combined sweep** : the tail follows the chosen A_t waveform and, simultaneously, the fin is held at the matching static bias A_f .

Each run starts with the robot already cruising straight. The bias command is then applied and the vehicle allowed to glide freely until it comes to rest. Overhead video provides trajectory, heading and yaw-rate data.

Propulsive turns. To quantify continuous turning while the fish was still generating thrust, the nominal sinusoidal tail command

$$\phi_t(t) = A \sin(2\pi f t)$$

was biased by a static offset $\Delta\phi_t$ so that the stroke became asymmetric, i.e. $\phi_t^{\text{turn}}(t) = \Delta\phi_t + A_t \sin(2\pi f t)$. The caudal fin was kept at an angle $\phi_t = A_t$. Four beat frequencies $f = \{0.50, 0.75, 1.00, 1.25\}$ Hz were combined with three peak tail amplitudes $A = \{20^\circ, 40^\circ, 60^\circ\}$. Each run lasted long enough for the robot to settle on a steady circular path. Overhead tracking yielded the (x,y) path and the yaw-rate ω .

4.3 Data processing

4.3.1 Data synchronisation, tracking and kinematic extraction

All on-board measurements (voltage, current, motor angles) and the overhead video share a common, absolute Unix-epoch clock synchronized by a 5 s LED flash at the start of every run. A

lightweight wrapper (ffmpeg drawtext) writes the time-stamp on each video frame, while the Raspberry Pi records the corresponding GPIO-26 state in the CSV log. Matching the video frame where the LED first lights with the epoch_us entry in the log yields a single offset; the residual timing error is below one video frame (< 33 ms).

Videos are then imported into Kinovea for planar calibration and semi-automatic point tracking. From the smoothed centre-of-mass trajectory, the speed $U(t) = \dot{s}$, acceleration, yaw angle and yaw rate $\omega(t)$ can be derived. These time-series are aligned to the Pi log with the LED offset and used directly for cost-of-transport, Strouhal and manoeuvre metrics.

4.3.2 Electrical power and cost of transport

The logger samples bus voltage V_k and current I_k at fixed intervals $\Delta t = 50\text{ms}$, so instantaneous electrical power is $P_k = V_k I_k$. Total energy for a run is obtained by discrete summation,

$$\mathcal{E} = \sum_{k=1}^N P_k \Delta t.$$

Cost of transport (CoT) normalises this expenditure by body weight and distance travelled,

$$\text{CoT} = \frac{\mathcal{E}}{mg\Delta d} \left[\frac{\text{J}}{\text{mkgN}} \right],$$

where m is the wet mass and Δd is the displacement measured during the steady-speed segment (acceleration and braking phases excluded).

The corresponding propulsive efficiency is simply the reciprocal of CoT,

$$\eta = \frac{mg\Delta s}{\mathcal{E}} = \frac{1}{\text{CoT}}.$$

4.3.3 Performance metrics

For every straight-line run the following scalars are stored:

$$\bar{U}, \quad \text{St} = \frac{2A_t f}{\bar{U}}, \quad \text{CoT}, \quad \eta_F = \frac{1}{\text{CoT}} \frac{1}{g},$$

Where η_f is a dimensionless number showcasing the propulsive efficiency (Froude). It tells intuitively how much energy ends up as useful translation.

For turning trials, positions $x(t), y(t)$ and yaw rate $\omega(t)$ are logged.

Chapter 5

Results

5.1 Propulsive Efficiency and Strouhal Number

5.1.1 Amplitude and frequency sweep

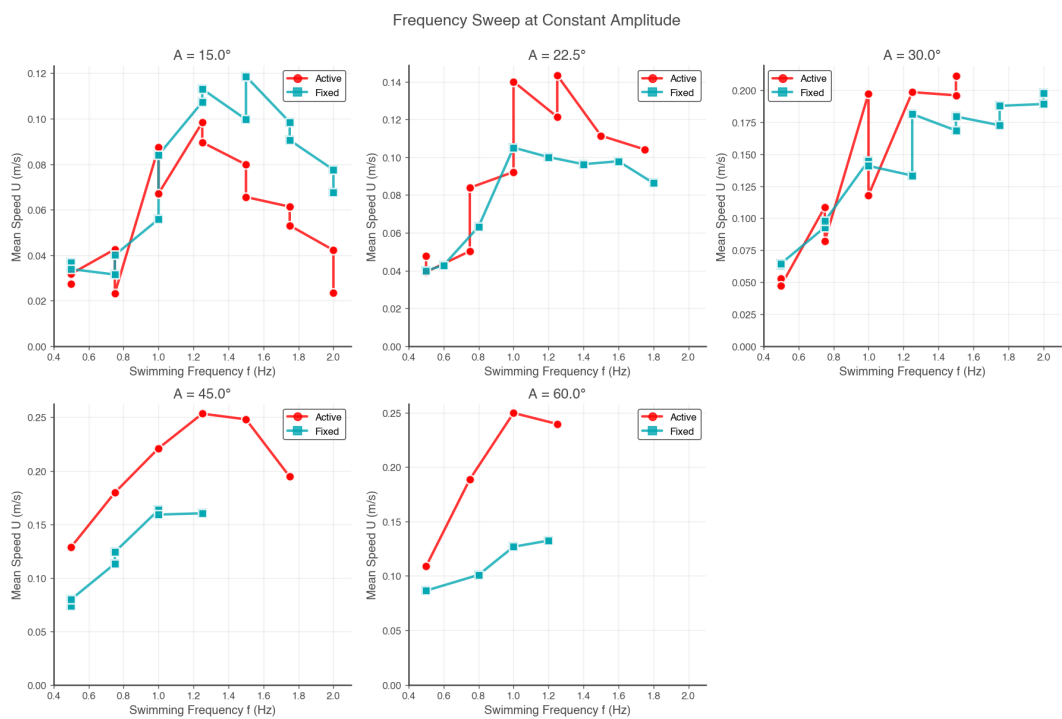


Figure 5.1: Mean forward swimming speed U plotted against tail-beat frequency f for trials at different tail oscillation amplitudes ($A = 15^\circ$ up to 60°), comparing Active (two-DOF) vs Fixed (single-DOF) caudal fin actuation.

The robot's cruising speed shows a clear peak at an optimal frequency for each amplitude. At low amplitude (15°), both active and fixed fin configurations achieve only modest speeds (≈ 0.1 m/s at best). The active-fin mode shows a slightly higher peak speed (around 0.11 – 0.12 m/s at $f \approx 1.25$ Hz) than the fixed tail (peak ≈ 0.10 m/s), followed by a drop-off at higher frequencies. With increasing tail amplitude, overall speeds rise and the benefit of active fin actuation becomes more pronounced. For example, at $A = 30^\circ$ and $A = 45^\circ$, the active tail attains higher top speeds (≈ 0.21 – 0.25 m/s) than the fixed fin (≈ 0.15 – 0.18 m/s) at their optimal frequencies. In these cases the active caudal fin generates more thrust, as seen by the upward shift of the red curves relative to blue.

Both configurations show that too high a frequency leads to reduced speed. This is likely due to ineffective stroke kinematics or increased drag at higher tail-beat rates. Notably, at the largest amplitude tested (60°), the active-fin robot reached ≈ 0.25 m/s at 1.0 Hz, whereas the fixed fin plateaued near ≈ 0.17 m/s. Thus, for moderate to large tail oscillations, active fin actuation consistently produces greater forward speed. Only at the smallest amplitude or at high amplitudes beyond optimum, the performance differences narrow.

Overall, the frequency sweep results show a strong dependence of cruising speed on tail-beat frequency, with a single peak, and demonstrate that adding an actively controlled fin joint improves the peak speed and attainable cruise performance.

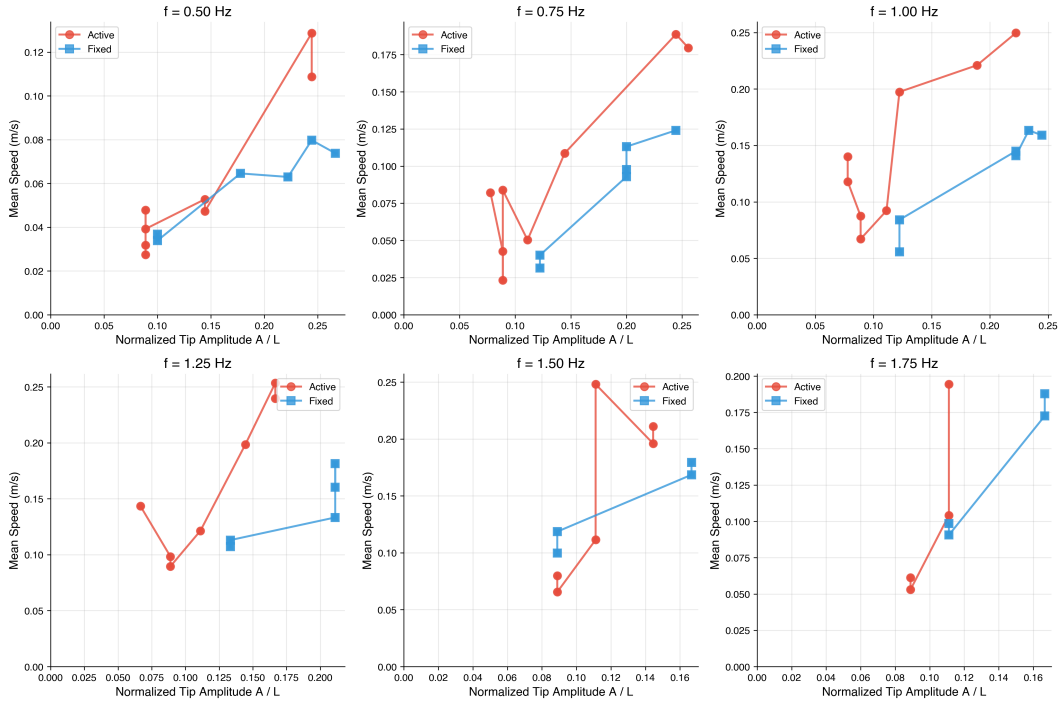


Figure 5.2: Mean forward swimming speed U plotted against normalized tail-tip amplitude A/L for trials at different frequencies.

The complementary view is given in Fig. 5.2: here each of the six sub-plots keeps tail-beat

frequency fixed (0.50–1.75 Hz) while the peak tip amplitude is varied in body-length units (A/L). Across all frequencies the speed curves shows a rise until about $A/L \approx 0.20$ – 0.25 , beyond which additional amplitude yields little or no gain and sometimes a slight decline.

The benefit of the second degree of freedom appears again. At every frequency the *active* fin lies above the *fixed* fin. The gap widens as amplitude approaches the plateau, reaching 35–40 % speed advantage at $f = 1.0$ – 1.25 Hz and $A/L \geq 0.2$. At the lowest frequency ($f = 0.5$ Hz) both modes are speed-limited by insufficient tail power, yet the active case still show better performance once $A/L > 0.15$. These observations corroborate the frequency sweep: two-DOF actuation makes large strokes profitable by redirecting lateral momentum into thrust rather than side-to-side movement.

Taken together, Figs. 5.1 and 5.2 show that the prototype's best cruise performance clusters around $f = 1.0$ – 1.25 Hz and $A/L \approx 0.20$ – 0.25 .

5.1.2 Strouhal and efficiency

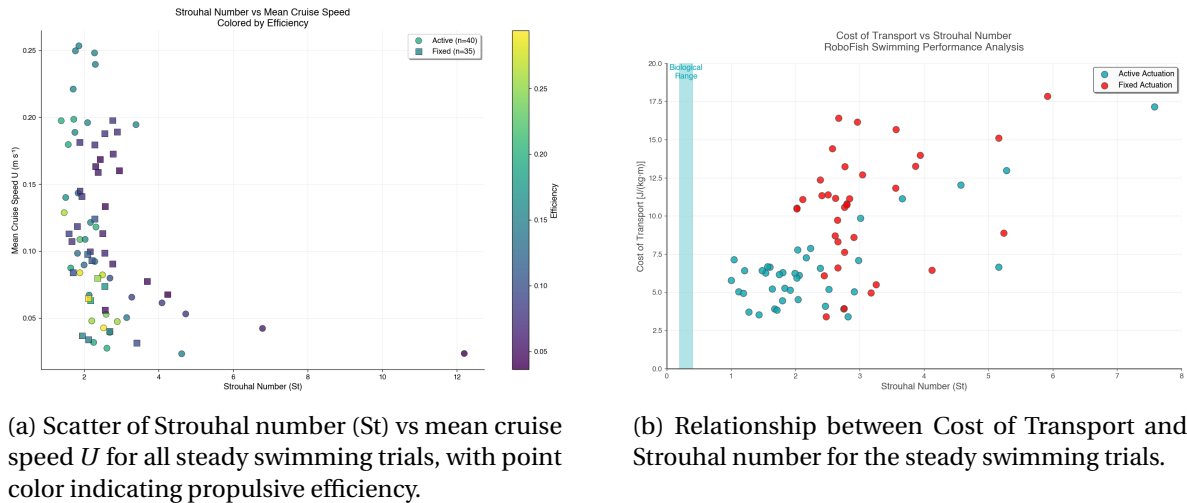


Figure 5.3

The figure 5.3a highlights the kinematic regime of the robotic fish. The Strouhal number, defined as $St = f \cdot A_{\text{tip}}/U$ (using peak-to-peak tail tip amplitude), ranges between about 1.5 up to 8–12 in the experiments – an order of magnitude above the $St \approx 0.2$ – 0.4 range typical of efficient biological swimmers. At higher cruising speeds ($U > 0.15$ m/s), the robot achieves its lowest Strouhal values (1.5–3). Conversely, tests that resulted in very low speeds (below 0.05 m/s) show extremely high St , indicating highly inefficient swimming. The point colors reveal that cases with lower Strouhal (2–3) tend to have higher efficiency, whereas trials with very high Strouhal (>5) yielded poor efficiency. The active-fin swims is more present in the upper-left region. The fixed-fin data (squares) cluster more toward moderate speeds (0.1 m/s) and often higher Strouhal values for the same speed,

indicating higher cost. Still, both modes show the same inverse relationship: as the robot swims faster (increasing U), the Strouhal number drops, but in all cases St remained well above 0.5, never approaching the 0.3 optimum seen in real fish. This suggests that the robot was operating in a lower-performance regime. The efficiency-colored trends support this: the best efficiencies achieved were around 20–25%, much lower than the 70–80% propulsive efficiency that a fish can reach within the optimal Strouhal band. The Strouhal-speed plot indicates that the two-DOF robotic fish did improve performance relative to the one-DOF case, but its kinematics still lie outside the biologically optimal Strouhal range.

In fig. 5.3b all robot data fall to the right of the cyan “biological range” band, underscoring that the robot swam with much higher Strouhal numbers than fish. The lowest CoT values achieved were around 3–5 (J/kg·m), and these occurred at the lower end of the Strouhal spectrum ($St \approx 1.5\text{--}2.5$) in the active-fin mode. In contrast, at very high Strouhal ($St > 5$), the cost of transport shoots upward. The active caudal fin generally reduced the cost of transport relative to the fixed fin, especially in the moderate Strouhal range (2–3): many active-fin runs lie around 5–8 (J/kg·m) in this regime, whereas the fixed-fin points at similar St often have CoT in the 8–12 range. For example, at $St \approx 2.2$, active actuation yielded $CoT \approx 6$ (J/kg·m) whereas the fixed tail was around 10 (J/kg·m). This indicates an efficiency gain with the second degree of freedom. The robot, constrained by its design could not reach that regime. The negative correlation between Strouhal and efficiency is consistent with prior studies: operating outside the optimal Strouhal leads to extra hydrodynamic losses.

In summary, the CoT vs St analysis reinforces that active fin control improved the robot’s energy economy at a given oscillation regime, but in absolute terms the robot’s cost of transport remains much higher than that of efficient swimming animals, corresponding to its high Strouhal operation.

5.2 Effect of Fin–Body Phase Lag

As shown in fig. 5.4, the relative phase angle between tail and fin significantly alters both forward speed and propulsive efficiency. The highest average swimming speed (approximately 0.3 m/s) was achieved when the tail oscillation led the fin oscillation by about 30°–50° (the fin’s motion lagging slightly behind the tail’s motion). This optimal phase offset coincided with a lower cost of transport, indicating that this coordination not only produced the fastest swimming but also showed efficiently. In contrast, when the phase relationship was reversed ($\phi > 0$) performance deteriorated sharply. At large fin-leading phase angles, forward velocity dropped to near zero and the energetic cost spiked (Fig. 5.4, right), underscoring the detrimental effect of this misalignment. A zero phase difference (tail and fin fully in-phase) yielded intermediate results in both speed and cost. These results demonstrate that a modest tail-leading phase creates constructive hydrodynamic interference between the tail and fin. It is allowing the fin to reinforce the tail’s shed vortices, thereby enhancing thrust and swimming speed. Conversely, a fin-leading phase (tail lag) appears to induce destructive interference mainly inducing side-to-side movement instead of generating thrust.

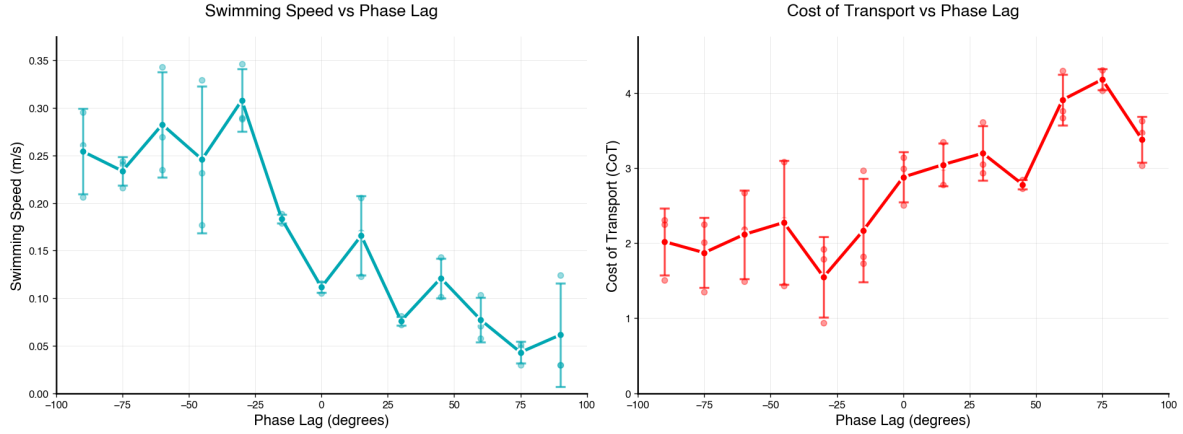


Figure 5.4: A parametric sweep of the phase difference between tail and fin actuations plotted against speed and Cost of Transport.

5.3 Maneuverability Tests

5.3.1 Gliding Turns

In these tests the robot executed a rapid tail deflection and then coasted, producing an inertial turn (“gliding”). This figure shows that combining the tail’s two degrees of freedom yields the highest turning rates. At a small flick of 15° , using only the tail produced a negligible yaw velocity (≈ 4 deg/s) and using only the fin joint was similarly low (≈ 5 deg/s). But when both joints were actuated together, the yaw rate more than doubled (≈ 10 deg/s). This trend continues at larger deflection angles. Notably, the tail-base joint contributes more to turning than the fin alone – the red curve is higher than purple at all points – indicating that swinging the larger caudal peduncle has a greater moment effect on the body. However, the simultaneous use of fin and tail amplifies the yaw beyond either individually, demonstrating a clear synergy between active body bend and fin deflection. The gain from the fin is especially evident at smaller angles (e.g. +100% increase at 15°), while at the largest angle the combined yaw rate is less than the linear sum of tail and fin alone. This suggests there may be some saturation or interference at extreme deflections (for instance, the tail and fin motions might partly oppose each other’s flow at 60°).

Across all amplitudes the two-DOF actuation enabled faster reorientation. These gliding turn tests illustrate that the additional fin joint can substantially improve instantaneous maneuverability, effectively letting the robot execute quicker turns by combining a body flip with a fin flick.

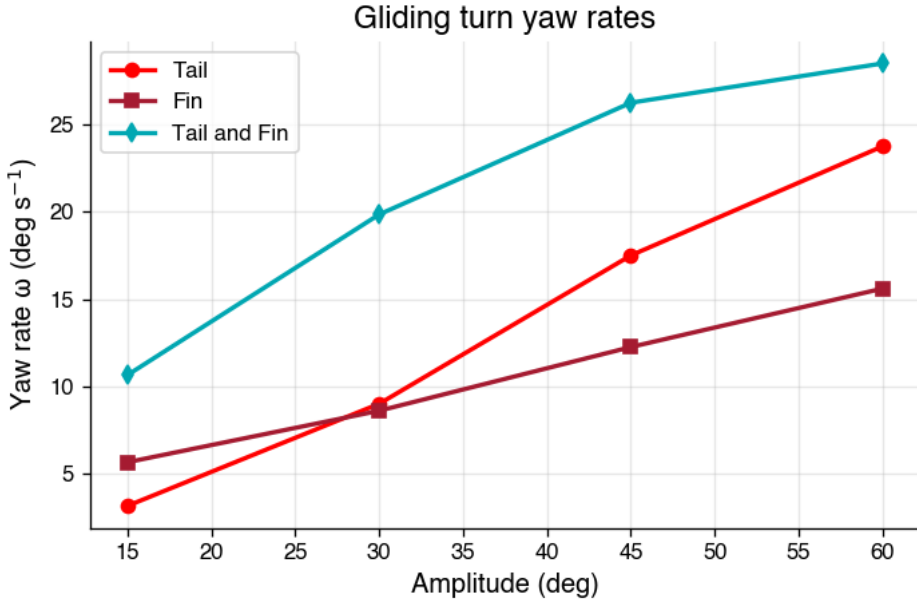


Figure 5.5: Mean yaw rate ω during a turn vs flick amplitude for three actuation modes. Red circles: tail-base actuation only; dark-red squares: fin (tail-tip) actuation only; cyan diamonds: combined tail + fin actuation.

5.3.2 Swimming Turns

In a separate experiment, the robot performed continuous swimming turns under tail-beat actuation, to mimic a fish steadily steering while propelling itself. The tail oscillation amplitude (20° , 40° , 60°) and frequency (0.5 up to 1.25 Hz) were varied, with the tail beating asymmetrically to induce a turn. The fin was set and kept in position at an offset of the same amplitude as the tail beating. The resulting trajectory paths (shown in fig 5.6) show that the turning radius depended strongly on tail amplitude and frequency. At the smallest tail amplitude, the robot could only execute very broad turns: at high frequency the path radius was large, essentially struggling to turn. Lowering the frequency to 0.5 Hz helped a 20° tail produce a somewhat tighter curve (since forward speed dropped, giving more time to yaw per stroke), but the turn was still relatively wide. In contrast, with the largest tail amplitude (60°), the robot achieved much sharper turns – the 60° tail sweeps produced smaller-radius loops, staying within a few tens of cm of the starting point for $f = 0.5\text{--}0.75$ Hz. Qualitatively, higher frequencies led to larger turning circles, whereas higher amplitudes yielded tighter turns (because large lateral tail strokes generated greater yaw per cycle). For example, an $A = 40^\circ$ tail at 0.75 Hz traced a moderate loop (turn radius on the order of ≈ 1 m), whereas $A = 40^\circ$ at only 0.5 Hz traced a tighter curve. The extreme case was $A = 60^\circ$ at low frequency: the robot almost pivoted around a point, showing very pronounced turning ability with minimal forward motion. These observations indicate a trade-off between maneuverability and speed in continuous turning. To turn sharply, the robot must oscillate its tail with large amplitude and/or at lower beat frequency.

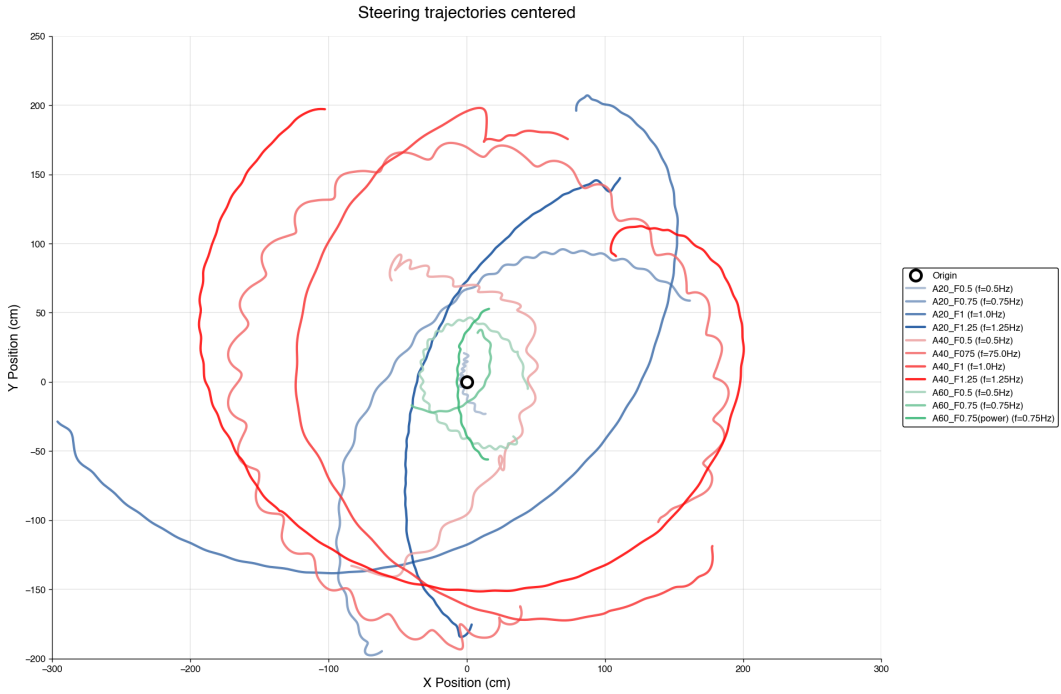


Figure 5.6: Continuous turning path for 20° tail-tip amplitude (shades of red), 40° (shades of blue) and 60° (shades of green) over various frequencies (0.5, 0.75, 1, 1.25)

(sacrificing translational speed), whereas high-frequency small-amplitude swimming favors going straight with only gentle curvature.

Finally, the cycle yaw kinematics during propulsive turns provide insight into how the robot's yaw rate oscillates within each tail-beat cycle. In these tests, the focused was on three tail amplitudes and varied the frequency. The yaw rate $\omega(t)$ was recorded over each cycle and normalized (0–100% of the tail beat period) for comparison. The traces revealed that at lower frequency (0.5 Hz) and larger amplitude, the robot's yaw rate swings strongly to either side during a cycle. For example, at $f = 0.5$ Hz with $A = 60^\circ$, ω reached about +45 deg/s at one phase of the stroke and -40 deg/s half a cycle later, crossing through zero (meaning the robot first yaws one direction then briefly yaws the opposite way later in the stroke). This reflects a “wiggling” turn: the body momentarily overshoots due to inertia and the large lateral tail throw, causing a reversal in yaw direction before the end of each cycle. But, an integration over time of the yaw rate would give a net change of direction at the end of each cycle. The smaller amplitude ($A = 20^\circ$) at 0.5 Hz showed the same general pattern of oscillatory yaw but with lower magnitudes (peaks around ± 20 deg/s). At a higher frequency of 1.0 Hz, the yaw rate traces became more one-sided. The robot still yawed predominantly toward the intended turn direction, but the opposite side excursion was much reduced. For instance, at $f = 1.0$ Hz, the $A = 40^\circ$ case saw a peak yaw rate of about -60 deg/s in the middle of the power stroke, and only a small counter-yaw of +25 deg/s later in the cycle. For the $f = 1.25$ Hz runs, the yaw rate profile is almost doubled in the turning direction compared to the reversal rate.

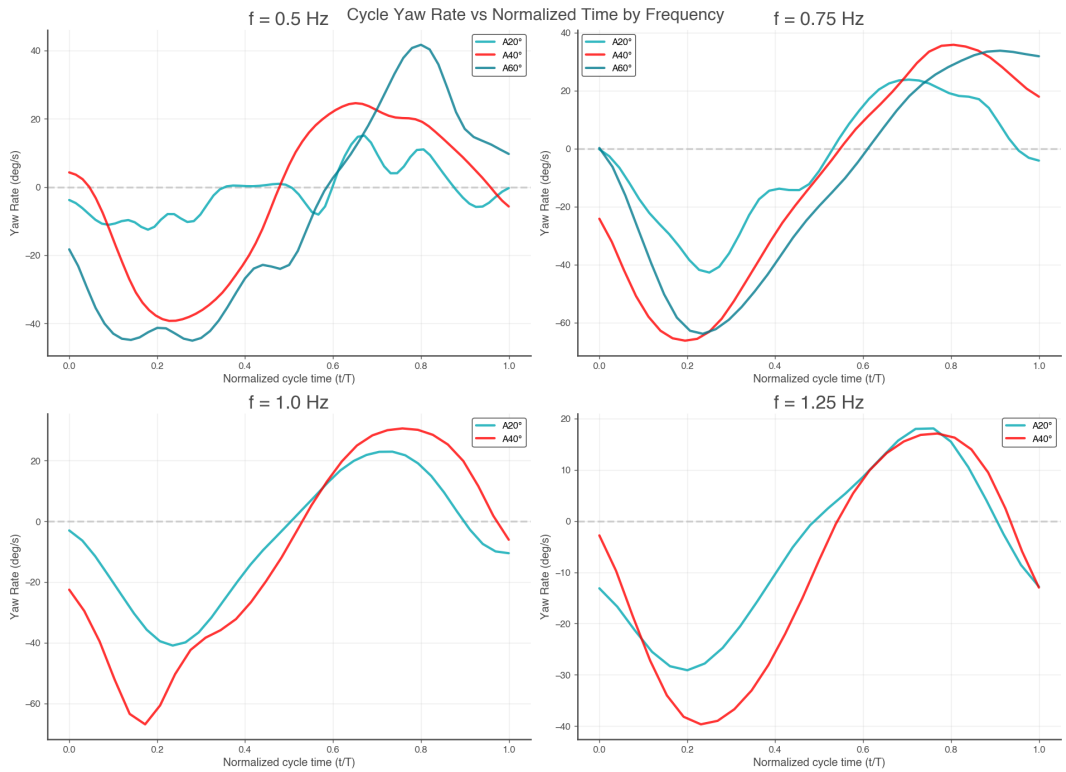


Figure 5.7: Yaw rate during one cycle for multiple frequencies and tail-tip amplitudes

In summary, high-frequency turning yields a smoother, more unidirectional yaw motion each cycle, whereas low-frequency, large-amplitude tail beats cause pronounced yaw oscillation . This is analogous to how real fish might experience body recoil at low tail-beat rates.

Chapter 6

Discussion

6.1 Steady Swimming: 2DOF Advantage and Strouhal Analysis

The above results demonstrate that adding an active second degree of freedom in the caudal fin significantly enhances the robotic fish's straight-line swimming performance compared to its 1DOF counterpart. The active tail fin allows the robot to achieve higher speeds at a given tail-beat frequency and amplitude, and to do so more efficiently, than the equivalent single-joint ("fixed fin") configuration. This is consistent with the idea that real fish benefit from flexible or actively controlled tail fins to boost thrust production [12]. In the experiments, the active-fin robot's peak cruising speed reached ≈ 0.25 m/s (at $A = 60^\circ$, 1 Hz), roughly a 40–50% increase over the fixed-fin case at similar tail kinematics. Likewise, cost of transport was reduced (from $\approx 8\text{--}12$ down to $\approx 5\text{--}6$ (J/kg·m) in mid-range conditions) with active actuation. One can ask why the second joint confers such benefits. One reason is that an actively controlled fin can maintain a more optimal hydrodynamic angle of attack and timing throughout the stroke. In the fixed-tail mode, the tail's trailing edge is effectively rigid and as frequency increases, flow separation may occur sooner and thrust does not scale up proportionally. In contrast, the active fin can correctly phase its motion to shed larger, more coherent vortex rings that carry momentum. This likely explains the higher peak speeds observed with the active tail. Moreover, an active fin can tune the effective stiffness of the tail: it can mimic a flexible foil that automatically bends at the right time. Prior studies on robotic swimmers have noted that a passively flexible tail can improve efficiency if driven near its resonant frequency [12], but if driven off-resonance it can actually reduce thrust. The active fin essentially allows to approximate an adaptive flexibility. It can actively bend to suit the frequency. This may be why the active system did not suffer the performance drop-off that the fixed tail showed at high frequencies, or at least showed less negative effect. It was observed that at the high frequency and low amplitude, the active tail's performance converged with or even dipped below the fixed tail's. This could be due to limitations of the actuator or controller at very rapid oscillations, leading to slight phase lags

or inability to hold the required fin angle, thereby diminishing the thrust advantage. It might also indicate that at very high flapping frequency, the flows are highly unsteady and turbulent such that extra fin motions yield no benefit. Overall, across the tested range the trend was clear: active fin control enables both higher speed and efficiency compared to the single DOF configuration.

Despite these improvements, the robotic fish still did not reach the low Strouhal numbers or high propulsive efficiency of real fish. The Strouhal-speed plot showed all data at $St \approx 1.5$ and above, whereas live fish (especially carangiform swimmers of similar size) typically cruise around $St = 0.25\text{--}0.4$ for maximal efficiency. The most efficient runs achieved were at $St \approx 2$, with a propulsive efficiency on the order of 20–25%. In contrast, a tuna or mackerel operating at optimal Strouhal can exceed 70% efficiency. There are several reasons for this gap. First, this first iteration of this 2-DOF fish is far from perfect in an hydrodynamic point of view. Floating devices on top of the fish created an enormous amount of drag. But the highest drawback in term of design is without a doubt the absence of a semi-rigid skin on the tail. The vortex shedding usually takes place around the body and travels with the undulation to the caudal fin, but in our case the rib-like structure of the tail breaks that smooth flow reducing the efficiency. As a result, the robot had to “over-flap” (high $f A/U$ ratio) to generate enough thrust to overcome drag, hence the high Strouhal values. Moreover, the test setup is not ideal for a 1+ meter fish because of the proximity to the walls. Tank confinement increases the hydrodynamic resistance, forcing the robot to spend extra power for the same speed thus reducing efficiency. This negative effect is particularly present within one body-length of the walls. Second, the control constraints play a role in this efficiency gap. The fin was operated in a simple sinusoidal motion with a fixed phase (90°) relative to the tail. It's possible that more sophisticated control (e.g. adjusting fin-tail phase dynamically) could achieve a lower effective Strouhal. Indeed, animals actively control their fin motions in response to flow conditions [13], and this may let them stay in the optimal zone. The robot's control was open-loop and not optimized in real-time. Future work could implement feedback to adjust tail beat kinematics on the fly to target a desired Strouhal or other efficiency metric. Finally, motor power and friction in the robot might have limited its effective output. Propulsive efficiency based on mechanical output vs electrical input were measured. Losses in gearing, minor tail oscillation asymmetries, and other inefficiencies kept the absolute efficiencies low. While the dual-DOF actuation improved performance, bridging the remaining efficiency gap to biological systems likely requires both better materials (for higher Reynolds and more elastic energy return) and improved gait strategies. Future improvements to the robot's tail structure could increase the diameter of the fiberglass rods. This could substantially improve the tail's structure, reducing unwanted motion in response to disturbances. A higher flexural rigidity should not decrease efficiency since most of the work done to bend the tail is elastically given back (except minor internal friction within the rod).

It is notable that the highest speeds were obtained at a specific combination of tail amplitude and frequency, beyond which adding frequency actually reduced performance showing the existence of a “sweet spot” in gait. This mirrors findings in other robotic swimmer studies: there exists a trade-off between speed and efficiency, and an optimal tail oscillation amplitude for maximal speed

at a given frequency [13]. For example, Anastasiadis et al. (2023) report that stride length (speed per frequency) peaks at a certain tail amplitude, whereas cost of transport monotonically worsens with larger amplitude. The results align with this: pushing amplitude to 60° yielded diminishing returns in efficiency even as it gave the highest speed. Eventhough energetically less efficient, higher frequency or amplitude is commonly used in biology over a short period to increase speed. Fish could flap harder to go a bit faster, but they usually don't, because it's energetically wasteful outside the optimal range. The robot was pushed to its mechanical limits and thus operated in a regime that real fish avoid. This highlights how biology has optimized a balance. Animals choose a tail-beat pattern that gives good enough speed for minimal energy, whereas the robot in its fastest mode chose high thrust at great energy cost. In short, the discussion of Strouhal and CoT underscores the importance of proper kinematics. Achieving fish-like efficiency will require not just adding an additionnal degree of freedom, but improving hydrodynamics, reducing mechanical friction along the transmission chain and having a fine-tuned control strategy.

6.2 Maneuverability and Gait Modulation

Beyond straight-line swimming, this study explored how the two-DOF tail impacts maneuverability, specifically turning performance. The data from both gliding turns and powered turns consistently show that the active fin greatly augments yaw control. In the gliding turn tests, for instance, combining tail and fin motion roughly doubled the achievable yaw rate compared to using the tail alone. This demonstrates the value of having multiple control surfaces. The tail base can give a large initial momentum, and the fin can fine-tune or add to the rotational impulse. Biomechanically, this is analogous to how real fish often use a sudden body bend (a C-bend) combined with a flick of their tail or fins to initiate rapid turns. The robot's fastest inertial turn (≈ 28 deg/s at 60° flick) is still far slower than the rapid turning maneuvers observed in fish escapes (where yaw velocities can reach hundreds of deg/s in a fraction of a second). However, it is an improvement over the single-DOF case and highlights a qualitative shift: the 2DOF tail enables a coupled bending motion that produces a stronger torque on the body. This reflects findings in fish biomechanics that suggest coordinating body and caudal fin motion yields the quickest turns.

In continuous turning (steering while swimming), the two-DOF tail showed its strengths. The robot could execute sustained turns of varying radii by biasing its tail oscillation. Here a clear trade-off between forward speed and turning sharpness emerged. With a large tail amplitude, the robot generates large lateral forces each half-cycle, yielding a strong yaw moment, but this also means more of the tail's energy goes into turning rather than propelling forward, so the forward speed is lower. Conversely, at higher tail frequencies, the forward thrust increases faster than the yaw per cycle, resulting in wider turns. The results quantitatively illustrate this: at $f = 1.25$ Hz and moderate amplitude, the robot covered ground more quickly but barely curved, whereas at $f = 0.5$ Hz and large amplitude it turned nearly on the spot (but moved slowly). Traditional single-actuator fish robots,

especially those designed for high cruising speed, tend to have poor turning ability. The tail structure do not help, the yaw gained at the first half cycle is quickly lost in the second part fo the cycle. By contrast, multi-actuated or more flexible-bodied robots achieve better maneuverability. The two-DOF caudal mechanism is an attempt to bridge this gap by adding maneuvering capability to a simple oscillating tail without heavily compromising the oscillation frequency. Using the additional degree of freedom to form a spoon shape at the end of the tail generates more yaw at the first half-cycle and do not give back as much as a single-DOF in the second half, pushing water behind rather than side to side.

The fact that the two-DOF tail can be driven in different gait modes (high-frequency small-amplitude vs low-frequency large-amplitude, and anything in between) shows a wide maneuvering package. The 2DOF tail provided the flexibility to access both regimes, it could deliver a big impulsive turn (tail + fin flick) or sustain a gradual turn (constant biased oscillation). A single-DOF tail would be less effective in the impulsive case and also somewhat limited in the continuous case since it would produce weaker yaw moments at equivalent amplitude because the lack of fin means less effective lateral area. Thus, the dual-actuated design improves maneuverability, both instantaneous and sustained.

It's important to note some limitations in the turning experiments. The power consumption was not measured during the turns, so the comparaison between the energy efficiency of different turning gaits is missing. For instance, is a gliding turn (coast after a flick) more energy-efficient than a continuous powered turn of the same net rotation? Intuitively it might be. The results qualitatively show the kinematic outcomes (faster turn vs slower), but an energetic analysis would be more insightful. Additionally, the motion capture tracked the fish in essentially a 2D plane (heading and position in horizontal plane). Any pitching or rolling motions during aggressive turns were not captured, though no observaton of obvious large out-of-plane motion was made. Real fish, however, often roll into a turn or pitch up/down. The robot lacked active fins like dorsals or pectorals to control and stabilize those motions.

Finally, the role of the active fin in maneuvering can be discussed compared to fish biomechanics. In nature, many fish have a fin or finlet that moves during turns, for example sharks can warp their caudal fin tips, and many fish deploy dorsal or anal fins asymmetrically to assist a turn. The active caudal fin essentially functioned as a rudder, augmenting the yaw torque. It can be seen that especially in gliding turns, the fin's contribution was significant at small amplitudes (where the main tail alone had little effect). This suggests a control strategy: for minor course corrections or low-speed turns, the robot could use primarily the fin flick (which might disturb forward motion less), whereas for rapid, large-angle turns, using both joints is better. The ability to differentially employ the two DOFs could allow nuanced control that can be further studied with close-loop feedback.

Chapter 7

Conclusion

This thesis investigates whether adding an actively controlled caudal-fin joint to a tendon-driven robotic fish could measurably enhance propulsive efficiency and manoeuvrability when compared with an identical single-DOF tail. Across fifty-plus steady-swimming trials the two-DOF configuration consistently delivered higher peak speeds (up to 0.25 m/s, ≈ 1.3 BL/s) and a 30–40% reduction in cost of transport at the most favourable kinematics ($f \approx 1$ Hz, $A/L \approx 0.22$). These gains confirm that coordinated tail-fin phasing can redirect lateral momentum into a more axial jet, recovering thrust that is otherwise lost in a rigid-fin design. A systematic phase sweep revealed that a tail-leading phase of roughly -30° to -50° maximises both speed and energetic economy, whereas a fin-leading phase quickly degrades performance. A direct evidence that constructive vortex interference is a narrow window that must be actively maintained.

Turning experiments further highlighted the value of the additional joint. In gliding turns, combining a tail flick with a synchronous fin deflection doubled peak yaw rate relative to the tail-only case, while continuous powered turns demonstrated that the robot can trade speed for radius in a controllable manner: large-amplitude, low-frequency strokes produced near-pivot turns, whereas high-frequency, small-amplitude gaits favoured wide, fast arcs. These behaviours mirror those observed in carangiform fish and show that meaningful agility can be achieved without resorting to a fully segmented body.

Despite these encouraging results the robot remains far from the biological performances. All tests operated at Strouhal numbers above 1.5, well outside the 0.25–0.40 optimum where many fishes reach 70%+ propulsive efficiency. Three factors explain this gap. First, hydrodynamic drag is inflated by the rib-like tail skeleton and external buoyancy modules; a continuous skin and streamlined fairings would reduce form drag and allow the same thrust to translate into higher speed and lower CoT. Second, mechanical friction and compliance in the tendon-pulley train dissipate energy and blur the commanded kinematics; stiffer rods, low-stretch cables and improved transmission chain should raise mechanical efficiency. Third, the present controller runs open-loop with a fixed

sinusoid. Closed-loop adjustment of amplitude, frequency and phase to maintain a target Strouhal or exploit resonance could unlock further gains, as biological swimmers do.

Accordingly, the present study should be viewed as a first iteration. It demonstrates that a minimally more complex tail architecture leads to tangible benefits and, perhaps more importantly, provides a quantitative baseline for iterative improvements. Future work could couple refined hydrodynamics with feedback control and real-time power monitoring, paving the way toward robotic swimmers whose efficiency and agility approach those of their biological counterparts while retaining the robustness and simplicity demanded by practical AUV missions.

Bibliography

- [1] A. B. Phillips, M. Haroutunian, S. K. Man, A. J. Murphy, S. W. Boyd, J. I. R. Blake, and G. Griffiths. “Nature in engineering for monitoring the oceans: comparison of the energetic costs of marine animals and AUVs”. In: *Further Advances in Unmanned Marine Vehicles*. Ed. by G. N. Roberts and R. Sutton. Vol. 77. IET Control Engineering Series. Stevenage, United Kingdom: Institution of Engineering and Technology, 2012, pp. 373–405. DOI: [10.1049/PBCE077E\ch17](https://doi.org/10.1049/PBCE077E\ch17).
- [2] Dr. John Dabiri. “Bio-Inspired Ocean Exploration”. In: *23RD ANNUAL ROGER REVELLE COMMEMORATIVE LECTURE*. 2022.
- [3] Christophe Eloy. “Optimal Strouhal number for swimming animals”. In: *Journal of Fluids and Structures* 30 (2012), pp. 205–218. ISSN: 0889-9746. DOI: <https://doi.org/10.1016/j.jfluidstructs.2012.02.008>. URL: <https://www.sciencedirect.com/science/article/pii/S0889974612000503>.
- [4] Michael Sfakiotakis, David Lane, and John Davies. “Review of Fish Swimming Modes for Aquatic Locomotion”. In: *Oceanic Engineering, IEEE Journal of* 24 (May 1999), pp. 237–252. DOI: [10.1109/48.757275](https://doi.org/10.1109/48.757275).
- [5] Cheryl Wilga and George Lauder. “Biomechanics of Locomotion in Sharks, Rays, and Chimeras”. In: Mar. 2004, pp. 139–164. ISBN: 978-0-8493-1514-5. DOI: [10.1201/9780203491317.pt2](https://doi.org/10.1201/9780203491317.pt2).
- [6] Daniele Costa, Giacomo Palmieri, David Scaradozzi, and Massimo Callegari. “Functional Design of a Biomimetic Flapper: Proceedings of the 4th IFToMM Symposium on Mechanism Design for Robotics”. In: Jan. 2019, pp. 302–309. ISBN: 978-3-030-00364-7. DOI: [10.1007/978-3-030-00365-4_36](https://doi.org/10.1007/978-3-030-00365-4_36).
- [7] Wah Yen Tey and Nor Azwadi Che Sidik. “Comparison of Swimming Performance between Two Dimensional Carangiform and Anguilliform Locomotor”. In: *Advanced Research in Fluid Mechanics and Thermal Sciences* 11 (July 2015), pp. 1–11.
- [8] Yaohui Xu, Bingbing Dong, Changzhen Zheng, Qiyang Zuo, Kai He, and Fengran Xie. “A Novel Untethered Robotic Fish with an Actively Deformable Caudal Fin”. In: *Advanced Intelligent Systems* 5 (Sept. 2023). DOI: [10.1002/aisy.202300276](https://doi.org/10.1002/aisy.202300276).

- [9] Michael Triantafyllou and George Triantafyllou. “An Efficient Swimming Machine”. In: *Scientific American - SCI AMER* 272 (Mar. 1995), pp. 64–70. DOI: [10 . 1038 / scientificamerican0395-64](https://doi.org/10.1038/scientificamerican0395-64).
- [10] Yuhan Li, Jialei Song, Ling Yin, Bowen Jin, Bo Yin, and Yong Zhong. “Hydrodynamics and Musculature Actuation of Fish during a Fast Start”. In: *Applied Sciences* 13 (Feb. 2023), p. 2365. DOI: [10 . 3390 / app13042365](https://doi.org/10.3390/app13042365).
- [11] Ben Lu, Chao Zhou, Jian Wang, Zhuoliang Zhang, and Min Tan. “Toward Swimming Speed Optimization of a Multi-Flexible Robotic Fish With Low Cost of Transport”. In: *IEEE Transactions on Automation Science and Engineering* 21.3 (2024), pp. 2804–2815. DOI: [10 . 1109 / TASE . 2023 . 3269775](https://doi.org/10.1109/TASE.2023.3269775).
- [12] Megan C. Leftwich, Eric D. Tytell, A. H. Cohen, and Alexander J. Smits. “Wake Structures Behind a Swimming Robotic Lamprey with a Passively Flexible Tail”. In: *Journal of Experimental Biology* 215.3 (Feb. 1, 2012), pp. 416–425. DOI: [10 . 1242 / jeb . 061440](https://doi.org/10.1242/jeb.061440).
- [13] Alexandros Anastasiadis, Laura Paez, Kamilo Melo, Eric D. Tytell, Auke J. Ijspeert, and Karen Mulleners. “Identification of the Trade-off between Speed and Efficiency in Undulatory Swimming Using a Bio-Inspired Robot”. In: *Scientific Reports* 13.1 (Sept. 12, 2023), p. 15032. DOI: [10 . 1038 / s41598 - 023 - 41074 - 9](https://doi.org/10.1038/s41598-023-41074-9). URL: [https : // www . nature . com / articles / s41598 - 023 - 41074 - 9](https://www.nature.com/articles/s41598-023-41074-9).